Electronic structure and x-ray-absorption spectra of wustite $Fe_{1-x}O$

S.-H. Chou, J. Guo, and D. E. Ellis
Department of Physics and Astronomy, Northwestern University, Evanston, Illinois 60201
(Received 14 February 1986)

Electronic ground-state properties of $Fe_{1-x}O$ were calculated by the spin-unrestricted local-density self-consistent discrete variational method, with (20—30)-atom clusters embedded in the crystal. Charge and spin distributions were determined for both ideal and defective compounds with the rocksalt structure. Effective atomic valence states and local magnetic moments were compared with interpretations of Mössbauer and neutron magnetic scattering data. Densities-of-states (DOS's) analyses were carried out and compared with FeO valence-band photoemission and optical spectra. K-edge x-ray-absorption near-edge spectra (XANES) for Fe sites were generated, using a multiple scattering approach. The variation of DOS's and XANES with local atomic arrangement was investigated to provide indications of measurable effects of lattice relaxation and metal valence shifts around defects.

I. INTRODUCTION

Wustite, $Fe_{1-x}O$ with the rocksalt structure, has a wide range of homogeneity. At low temperatures it is unstable, decomposing into α-Fe and magnetite Fe_3O_4 below 843 K.[1,2] Metastable wustite can be produced by rapid quenching from high temperature, and charge balance dictates a certain fraction of Fe^{3+} ferric ion at a particular composition x. Deviation from stoichiometry mainly results from cation vacancies and interstitials, which exist in clustered form. It has been shown that the defect arrangement and electronic properties, including conductivity and magnetic mechanisms, are closely connected. Previous analysis of x-ray and electrical properties indicated that $Fe_{1-x}O$ is a small polaron conductor whose behavior can be described in terms of a cluster model.[3,4] It is antiferromagnetic with critical temperature $T_N = 198$ K, in contrast to ferromagnetic magnetite with critical temperature of 858 K.

In this paper, we use an *ab initio* local-density theoretical approach to study the electronic structure, magnetic, and spectroscopic properties associated with the "perfect" crystal, isolated vacancies, and defect clusters in $Fe_{1-x}O$. We employ molecular-cluster models of different local environments, and attempt to relate the theoretical charge and spin distributions and spectra to specific features of experimental data. X-ray-absorption near-edge spectra (XANES) are very sensitive to the local environment of the absorbing atom,[5] and Mössbauer data reflect the immediate environment of iron ions. The XANES and Mössbauer results are a superposition of several different metal environments.[6,7] We have previously shown how theoretical study can analyze each different metal environment separately and provide interpretation for the major features of XANES results in compounds.[5,8]

A brief description of the theories used for both ground-state self-consistent-field (SCF) electronic structures and XANES calculations is presented in Sec. II. In Sec. III we analyze our results and make comparisons with experimental data. The discussion and conclusions are included in Sec. IV.

II. THEORETICAL APPROACH

A. Embedded-cluster scheme

To describe the clustered cation vacancies and interstitial defect structures in wustite, we use the discrete variational (DV-$X\alpha$) embedded-cluster approach.[9–11] This model is both computationally convenient and accurate, as long as one uses a sufficiently large cluster to reproduce the features of the extended crystal. Clusters centered on a lattice site have a cubic structure of the form $AB_6A_{12}B_8\cdots$ while setting the origin at the tetrahedral interstitial site leads to clusters $XA_4B_{12}A_{12}\cdots$.

An antiferromagnetic compound cannot have the full translation symmetry of the lattice, requiring instead a larger superlattice unit cell to describe the alternating magnetic structure. For crystalline FeO below T_N, the superlattice unit cell contains eight Fe atoms (four spin up and four spin down), and eight O atoms, with Fe^{2+} spin moments lying parallel to [111], and adjacent (111) sheets having reversed orientation.[12] For present purposes we ignore the rhombohedral distortion accompanying the magnetically ordered phase. The corresponding cluster model can be described by D_{3d} symmetry. The energy, $\sim kT_N$, which is associated with the magnetic ordering, is typically around 0.01—0.1 eV per atom. If we are interested in electronic and optical[13] properties of wustite which involve energy scales much larger than 0.1 eV, then it is reasonable to ignore the superlattice structure and impose a symmetry equivalence on the outer-shell Fe atoms in our cluster models. Thus we may employ octahedral O_h symmetry instead of D_{3d} to calculate the crystalline FeO structure. In order to test this assumption, we did ground-state self-consistent-field (SCF) calculations for the ideal crystalline structure for clusters of both D_{3d} and O_h point-group symmetry.

Two cluster configurations are used in this work (Fig.

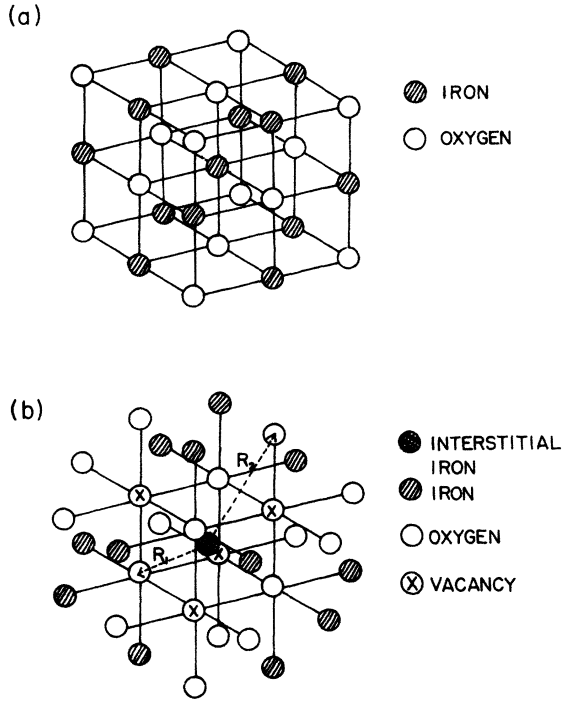

FIG. 1. Cluster models used in this work: (a) the 27-atom clusters of O_h ($FeO_6Fe_{12}O_8$) or D_{3d} ($FeO_6Fe_6Fe_6O_2O_6$) symmetry, with the z axis along the (111) direction, representing the perfect crystal, and (b) the 33-atom interstitial-vacancy complex ($FeX_4O_4Fe_{12}O_{12}$) of T_d symmetry.

1): (a) a 27-atom model of O_h symmetry, $FeO_6Fe_{12}O_8$, or D_{3d} symmetry, $FeO_6Fe_6Fe_6O_2O_6$, both representing the ideal crystalline structures; (b) a 33-atom model of tetrahedral (T_d) symmetry, $FeX_4O_4Fe_{12}O_{12}$, which represents the much discussed 4-vacancy 1-interstitial (4:1) defect cluster. Here, X denotes a cation vacancy. We also use a 37-atom model of T_d symmetry to simulate the relaxed defect cluster, $FeX_4Y_4O_4Fe_{12}O_{12}$, where Y denotes a virtual atom (empty site) at the original unrelaxed oxygen-atom position. For the defect cluster, the first-shell oxygen atoms [O(1)] are located at distance of 3.47 a.u. (unrelaxed), 3.82 a.u., and 4.16 a.u. (relaxed), respectively, from the central iron, Fe(1). The second-shell atoms [Fe(2) and O(2)] are held at a distance of 6.64 a.u. from the center.

The ground-state electronic structures of these clusters were first obtained using the self-consistent discrete variational (DV-$X\alpha$) method.[9–11] From density-functional theories, the approximate one-electron functions ψ_i satisfy the equation

$$h\psi_i=\varepsilon_i\psi_i \ , \tag{1}$$

where (in Hartree a.u.)

$$h=-\tfrac{1}{2}\nabla^2+V_C+V_{\rm xc}^{\sigma} \ , \tag{2}$$

$$V_{\rm xc}^{\sigma}=-3\alpha(3\rho_\sigma/4\pi)^{1/3} \ . \tag{3}$$

We use the Kohn-Sham value $\alpha=\frac{2}{3}$ in our calculations, σ represents spin, V_C and $V_{\rm xc}^{\sigma}$ are Coulomb and exchange-correlation potentials, respectively, and ψ_i are expressed as a symmetrized linear combination of molecular basis functions χ_j, which are, in turn, formed from a numerical atomic basis: $\psi_i=\sum_j\chi_jC_{ji}$. The linear variational procedure leads to the secular matrix equation to determine the variational coefficients $\underline{C}$, as

$$(\underline{H}-E\underline{S})\underline{C}=\underline{0} \ , \tag{4}$$

where

$$H_{ij}=\langle\chi_i\,|\,h\,|\,\chi_j\rangle, \quad S_{ij}=\langle\chi_i\,|\,\chi_j\rangle \ . \tag{5}$$

The integrations are performed in three dimensions with the quasirandom Diophantine method.

The cluster charge density, obtained from the eigenvectors, is expanded in a linear combination of basis functions which are centered around atomic sites. In the present work the charge and spin densities are projected onto superpositions of *spherical* radial densities centered on the nuclei. The expansion coefficients are obtained by a weighted Mulliken analysis of the eigenvectors,[14] and the potential thus obtained is called the self-consistent charge (SCC) potential.

Our clusters do not always contain an integral number of unit cells, and thus carry a net charge. Earlier calculations have shown that the self-consistent ionic charges are considerably less than the formal oxidation numbers.[11] In any case, charged defect clusters are accompanied by nearby compensating Fe^{3+} ions, to satisfy overall change neutrality and to minimize the electrostatic energy. Thus neutral defect clusters are employed in this work, with detailed computational parameters used in DVM calculations listed in Table I.

B. X-ray-absorption near-edge structure (XANES)

The total x-ray-absorption cross section integrated over cluster orientation, as well as the photoelectron polarization for K-edge photoionization, is[15–17]

$$\sigma(\omega)=\tfrac{4}{3}\pi^2\alpha\hbar\omega\sum_L\sum_{m_\gamma}|\,D_{Lm_\gamma}^{-}\,|^2 \ , \tag{6}$$

where $L=[l,m]$ and

$$D_{Lm_\gamma}^{-}=(-1)^{m_\gamma}(\tfrac{4}{3}\pi)^{1/2}\langle\phi_L^{(-)}\,|\,rY_{1m_\gamma}\,|\,\phi_{1s}\rangle \ . \tag{7}$$

m_γ is the projection of the dipole interaction operator along the cluster z axis, α is the fine-structure constant, and $\phi_L^{(-)}$ is a partial-wave component of the normalized final state. The final-state delocalized continuum wave functions required for the K-edge photoabsorption cross section cannot be easily calculated with a finite linear-combination-of-atomic-orbitals (LCAO) basis. Thus the fully-self-consistent SCC potential was truncated to muffin-tin form to make use of the more appropriate multiple-scattered-wave (MSW) method.[15–17]

For iron oxide compounds, the mean free path for low-energy electrons (i.e., with $E<100$ eV) is around 8 a.u.,[18] and the K-edge core-hole–lifetime width of Fe is around 1 eV.[19] Both factors strongly limit the range of the elastic scattering of the photoelectron. The inelastic scattering, multielectron excitation, and many-body effects in general

TABLE I. Model parameters employed in DVM calculations.

Cluster size	$FeO_6Fe_{12}O_8$	$FeO_6Fe_6Fe_6O_2O_6$	$FeX_4O_4Fe_{12}O_{12}$
Symmetry	O_h	D_{3d}	T_d
Number of integration points	7430	7435	8359
Size of crystal (atoms) included in potential	66	176	128
Exchange parameter $\alpha=\frac{2}{3}$			
Cell constant (Å)	4.32		
Frozen orbitals	Variational basis was explicitly orthogonalized against the core orbitals. Fe: $1s,2s,2p,3s,3p$ O: $1s$		
Thermal broadening	0.01 Ry. The Fermi-Dirac occupation numbers were broadened to accelerate iteration convergence and to reduce effects of small level shifts.		
Crystal pseudopotential	The periodic crystal potential V is constructed. Then, for all points $r_i<2.0$ a.u. (where $r_i=\|\mathbf{r}-\mathbf{R}_i\|$ and $\mathbf{R}_i$ is the position of an ion external to the cluster), V is truncated to -0.20 a.u. An effective repulsive core potential is thus empirically approximated.		

are not explicitly included in our single-particle picture. Since the Fourier transform of experimental XANES shows that the main features are generated by scattering of the photoelectron from the first few shells of neighboring atoms,[6,20] it seems reasonable to include only the first few shells in our theoretical cross-section models.

Due to the short mean free path, there is very little chance for a K-edge photoelectron to escape the bulk system to the vacuum. The asymptotic potential for the photoelectron in this system should be approximately the ground-state muffin-tin constant potential V_{MT}, not the vacuum limit $V=0$. We constructed an outer-sphere (OS) potential, which falls Coulombically outside the cluster-enclosing radius R_{OS}. The potentials of atoms outside the outer sphere were thus omitted in the multiple-scattering wave-function calculation, but were included in the SCF procedure.

III. RESULTS

A. Charge and spin distribution

1. *Defect-free structure*

The SCF ground-state results for 27-atom clusters, both with and without superlattice structure, are summarized in Table II. Volume charge is defined here as that charge contained in the region of space closest to a given atom, in analogy to the Wigner-Seitz construction. From the volume charge of Fe(1) and O(1), one can see that oxygen atoms in wustite are much less sensitive to the magnetic order than the iron atoms. As we change symmetry from O_h (paramagnetic) to D_{3d} (antiferromagnetic), the central-iron nearest-volume charge changes from $1.15e$ to $1.49e$, while the volume charge of the first-shell oxygen atoms is unchanged, $-1.16e$. One would expect the volume charge of second-shell iron atoms with spin up to be equal to those with spin down in the cluster with D_{3d} symmetry, but our results suggest charge transfer onto the ↑-spin sites, and onto O(2). The weighted average volume charges for second-shell iron and oxygen are $+1.13e$ and $-1.00e$, respectively, for the cluster with D_{3d} symmetry. These are nearly (within $0.11e$) the same as the results of the cluster with O_h symmetry. For both models with O_h and D_{3d} symmetry, the absolute values of the volume charge of the first-shell atoms are larger than those of the second-shell atoms. This is an example of finite-cluster-size effects, and also relates to the different sampling volumes for interior and "surface" atoms.

The Mulliken populations for charge density of the cluster with D_{3d} symmetry are nearly (± 0.05) the same as those corresponding results of the cluster with O_h symmetry. Thus the reorientation of Fe(2) spins permitted by the superlattice structure has a minimal influence on the

TABLE II. SCF ground-state charge and spin distribution for ideal crystalline 27-atom FeO clusters with and without magnetic superlattice structure. Here, Fe(1) and O(1) indicate those iron and oxygen atoms which are closest to the cluster center, and Fe(2) and O(2) mean those atoms second nearest to the center. Fe(2↑) means those iron with majority electrons of spin up. O(2z) means those oxygen atoms located on the z axis, along the (111) direction.

Cluster size			$FeO_6Fe_6Fe_6O_2O_6$		$FeO_6Fe_{12}O_8$	
Symmetry			D_{3d}		O_h	
Volume charge	Fe(1↑)		1.49		1.15	
	O(1)		−1.16		−1.16	
	Fe(2↓)		1.36		1.06	
	Fe(2↑)		0.90			
	O(2z)		−0.83		−0.89	
	O(2)		−1.06			
	Mulliken populations for charge and spin density					
			Charge	Spin	Charge	Spin
	Fe(1)	3d	6.34	3.03	6.33	2.89
		4s	0.44	0.06	0.42	0.06
		4p	0.40	0.06	0.43	0.08
	Total		+0.82	+3.15	+0.82	3.03
	O(1)	2s	1.90	−0.00	1.90	−0.01
		2p	4.67	0.03	4.69	−0.21
	Charge		−0.57	+0.03	−0.59	−0.22
	Fe(2↓)	3d	6.18	−3.46	6.20	−3.50
		4s	0.71	−0.16	0.67	−0.18
		4p	0.55	−0.15	0.53	−0.16
	Total		+0.56	−3.77	+0.60	−3.84
	Fe(2↑)	3d	6.19	3.48		
		4s	0.69	0.15		
		4p	0.55	0.15		
	Charge		+0.57	3.78		
	O(2z)	2s	1.89	0.01	1.91	+0.01
		2p	4.70	0.16	4.73	+0.06
	Total		−0.59	+0.17	−0.64	+0.07
	O(2)	2s	1.90	−0.00		
		2p	4.72	−0.05		
	Total		−0.62	−0.05		

LCAO description and the derived electrostatic potentials. Differences between the nearest-volume description and the LCAO analysis arise because of diffuse, overlapping orbital components, and remind us of the essentially arbitrary nature of any pantitioning scheme.

Concerning the spin distribution, we note the following:

(a) The central-site spin-only moment is found to be $3.2\mu_B$ in D_{3d} and $3.0\mu_B$ in O_h symmetry. The off-center iron moments are consistently about $3.8\mu_B$. These values can be compared with the estimate of $4.2\mu_B$ for Fe^{2+} ions used in fitting neutron magnetic scattering data.[12] The observed *reduced* scattering compared to that expected from Fe^{2+} moments was interpreted as evidence for local antiferromagnetic coupling between tetrahedral interstitial Fe^{3+} ions and nearest-neighbor octahedral iron atoms of both Fe^{2+} and Fe^{3+} character. The resulting cluster moment was suggested to lie in the (111) plane, with random orientation. Conflicting interpretations of Mössbauer data have been made, due largely to difficulties in preparing well-characterized samples. Extensive studies by Greenwood and Howe[7] lead to a picture of numerous inequivalent Fe^{2+} sites with 0.5–1.0 mm/sec quadrupole splitting due to adjacent vacancies or Fe^{3+} sites. Broadening of the lines is observed with increasing deviation from stoichiometry, i.e., with increasing defect concentration. Structure associated with Fe^{3+} sites is identified with both typical Fe^{2+} magnetic hyperfine splitting (340 kG) and Fe^{3+} splitting (480 kG) being resolved below T_N.

(b) Comparison of the spin distributions of O 2s and Fe 4s,4p orbitals between D_{3d} and O_h symmetry shows that they differ only by an amount of 0.01–0.03. However,

TABLE III. SCF ground-state charge and spin distribution for (4:1) tetrahedral defect clusters. Here, Fe(1), O(1), Fe(2), and O(2) have the same meaning as in Table II, and X denotes a Fe vacancy. Y denotes a virtual atom at the original unrelaxed [O(1)] positions.

Cluster		$FeX_4Fe_{12}O_{12}$		$FeX_4Y_4O_4Fe_{12}O_{12}$		$FeX_4Y_4O_4Fe_{12}O_{12}$	
Distance O(1)R_1	(a.u.)	3.47		3.82		4.16	
Volume charge	Fe(1)	2.26		2.58		2.60	
	X	−0.70		−0.75		−0.70	
	O(1)	−0.58		−1.32		−0.77	
	Fe(2)	1.19		1.06		1.10	
	O(2)	−0.81		−0.67		−0.68	
		Mulliken populations for charge and spin density					
		Charge	Spin	Charge	Spin	Charge	Spin
	Fe(1)	3d 6.18	−2.50	6.10	−3.55	6.15	−3.68
		4s 0.13	−0.03	0.33	−0.13	0.44	−0.03
		4p 0.23	−0.05	0.53	−0.02	0.55	−0.02
	Total	+1.46	−2.58	+1.04	−3.70	+0.86	−3.73
	X 1s	0.11	0.02	0.13	−0.04	0.13	−0.01
	2s	0.03	0.00	0.05	0.00	0.05	−0.00
	2p	0.11	−0.01	0.32	−0.06	0.31	−0.03
	Total	−0.25	+0.01	−0.50	−0.10	−0.49	−0.04
	Y 1s			−0.73	0.14	−0.72	0.07
	2s			0.16	0.00	0.21	0.01
	2p			0.21	0.10	0.08	0.09
	Total			+0.36	+0.24	+0.43	+0.17
	O(1)	2s 1.89	0.01	1.90	0.01	1.86	0.02
		2s 4.56	0.27	4.63	0.29	4.71	0.26
	Total	−0.45	+0.28	−0.53	+0.30	−0.57	+0.28
	Fe(2)	3d 6.06	3.74	6.05	3.75	6.06	3.71
		4s 0.70	0.15	0.70	0.11	0.68	0.09
		4p 0.58	0.22	0.60	0.16	0.61	0.15
	Total	+0.66	+4.11	+0.65	+4.02	+0.65	+3.95
	O(2)	2s 1.92	0.00	1.91	0.00	1.91	0.00
		2p 4.63	0.44	4.60	0.51	4.61	0.47
	Total	−0.55	+0.44	−0.51	+0.51	−0.52	+0.47

the 2p orbital of O(1) and the 3d orbital of Fe(1) spin moment vary by an amount of 0.18 and 0.14, respectively. This is consistent with the fact that the magnetic ordering of FeO and the Fe 3d populations are correlated. Also, there is strong hybridization between O 2p and Fe 3d orbitals.

(c) The magnitude of the second shell iron spin is around $(0.7-0.8)\mu_B$ larger than that of the central iron. This is characteristic of our finite-cluster-size model, with moments which increase toward the "surface." Although we use a potential-embedding scheme, the cluster-size effects associated with the outer atoms still are exhibited in the Mulliken populations and spin distribution, and also affect the density of states (DOS), as we will discuss later.

2. *Effects of cation vacancies and interstitial Fe*

Table III lists the SCC ground-state results of T_d vacancy-interstitial clusters with the first-shell oxygen atom unrelaxed at 3.47 a.u. and relaxed at 3.82, a.u. and 4.16 a.u. from the central iron. From these results, one can observe the following:

(a) The nearest volume charge of the central iron changes from 1.15e in the O_h cluster to 2.26e, 2.58e, and 2.60e in the T_d clusters. There is thus a charge transfer of $(1.11-1.45)e$ from the central iron to the neighboring atoms as the local symmetry of the iron changes from O_h to T_d, essentially representing the difference between divalent and trivalent configurations. This is consistent with many previous suggestions that Fe^{3+} occupies the interstitial sites.

(b) The volume charge of the cation vacancy X is insensitive to the changes of position of the first-shell oxygen atoms. Thus the O 2p valence band maintains nearly constant charge density at vacancy sites, while accepting charge from the interstitial ion.

(c) The distances between virtual atom Y and its nearest oxygen atom in the relaxed T_d clusters are 0.35 and 0.69

a.u., respectively. It is reasonable to combine the volume charges of Y and O(1) in the T_d clusters as a measure of the volume charges of the first-shell oxygen atoms. We see that the combined O(1) volume charges are not only sensitive to the number of nearest iron atoms, but they are also very sensitive to the distance to the central (interstitial) iron atom, with a maximum value ($-1.3e$) around the $R_1=3.8$ a.u. relaxed distance.

(d) The volume charges of the second-shell iron and oxygen atoms are relatively insensitive to the existence of the cation-vacancy-interstitial defect cluster, but do respond with charge transfers of $(0.1-0.2)e$.

(e) From the Mulliken populations, we can see that the occupation numbers of the diffuse $4s$ and $4p$ orbitals of the central iron atom are more sensitive to the variation of the first-shell oxygen-atom distance than the $3d$ orbitals.

(f) The central-iron-atom spin moment is sensitive to both its local-symmetry environment and the first-shell oxygen-atom distance. It was expected that the spin moment of iron would increase as its local symmetry changes from O_h to T_d. However, our results show that for the unrelaxed T_d defect cluster, the magnitude of the central-iron spin moment decreases by $0.45\mu_B$, and the increment of the spin moment is only found for the relaxed T_d defect clusters.

(g) The spin moments of the second-shell iron atoms show relatively weak response to the changes of the local symmetry and the first-shell oxygen-atom positions, as they are slightly larger than the values found for "ideal crystal" clusters.

B. DOS and the valence photoemission and optical spectra

1. Defect-free FeO

Figures 2(a)–2(f) show the theoretical DOS of a 27-atom ideal crystalline cluster with magnetic superlattice structure and D_{3d} symmetry. Figure 2(a) is the total DOS of this cluster. There are three main peaks below the Fermi-energy zero at 2.7, 4.4, and 6.4 eV. The ↑,↓-spin symmetry correctly characterizes this material as an antiferromagnet (AF). Experimentally, the x-ray photoemission spectrum of FeO (Refs. 21–23) shows four peaks: structures at 1.5, 4.3, and 7.8 eV are identified as originating from the Fe $3d$ orbitals, with a peak at 6.0 eV assigned to the top of the O $2p$ band.[23] To understand the correspondence between our theoretical results and the photoemission, we have to examine the DOS in more detail. Figure 2(b) shows the $3d$ DOS of the central iron, Fe(1). The filled ↑-spin band is broadened by interaction with the neighboring ions to a width of ~ 10 eV, while the partially occupied ↓-spin band lying above the O $2p$ states is more narrow and atomiclike. An intra-atomic exchange splitting of ~ 5 eV is evident. Figure 2(c) gives the $3d$ DOS of those outer iron atoms with the majority electrons spin down, while Fig. 2(d) gives the $3d$ DOS of those outer iron atoms with majority electrons spin up. Figures 2(c) and 2(d) are almost mirror images of each other, as one expects from the AF structure. However, they do not show the same broadening and detailed structures as for the central ion [Fig. 2(b)]. This demonstrates that although we embedded the cluster atoms in the crystal potential, the finite-cluster-size effects are still reflected in the DOS of the outer atoms in the cluster. By comparing Fig. 2(b) with photoemission spectra of FeO,[23] it is possible to see that Fe $3d$ peaks at 6.8, 2.7, and 0.7 eV correspond to the experimental structures at 7.8, 4.3, and 1.5 eV. The differences of 1.0, 1.8, and 0.8 eV are probably due to the fact that our results are from ground-state calculations. The relaxation energies associated with the Fe $3d$ photoemission may be of the order of 2 eV, according to our experience on similar systems. The $3d$ peaks at 5.6 and 6.8 eV can also be identified with photoemission structure around 6.0 eV, and arise from bonding interactions between Fe $3d$ and O $2p$ states.

Figures 2(e) and 2(f) show the DOS of $2p$ orbitals of O(1) and O($2z$), respectively (z denotes the z axis). The $2p$ DOS of O(1) shows prominent structures at 6.4, 5.2, and 2.3 eV. Experimentally, it was observed that the oxygen band is located at 5.5,[21] 7.3,[22] or 6.0 eV.[23] Comparison between the O(1) $2p$ DOS and the $3d$ DOS of Fe(1) shows that the $2p$ peak at 2.3 eV would be covered up by the strong $3d$ peak at 2.7 eV, and is not experimentally resolvable. The two $2p$ structures at 6.4 and 5.2 eV and an overall bandwidth of ~ 10 eV are thus in fairly good agreement with the photoemission data. Since the $2p$ orbitals of oxygen are very diffuse, the relaxation energies associated with an O $2p$ photoemission must be very small. The differences between Figs. 2(e) and 2(f) again reveal the line narrowing associated with "surface" atoms of the cluster.

Since the total DOS of a given cluster contains contributions from each atom in the cluster, and the outer atoms are the majority, the finite-cluster-size effects are also exhibited in the total-DOS results. Thus, interpretations of the total DOS are less reliable than of the DOS of interior atoms for bulk properties, and we will only describe the DOS of Fe(1) and O(1) in the following sections. We also note at this point that although $Fe_{1-x}O$ is a semiconductor, the "perfect-crystal" calculations do not display an obvious gap in the DOS around E_F. The cluster interlevel spacing of 0.2 eV at E_F may be compared with estimates of the semiconducting gap of ≤ 0.1 eV obtained from optical-absorption data[13] and hopping activation energies of 0.16 eV obtained from conductivity measurements.[4] The intense optical absorption is relatively featureless, indicating a high density of available states over a wide energy range. The broad maximum seen at ~ 1.3 eV is apparently associated with transitions into the minority-spin $3d$ band; see Fig. 2(b).

In order to determine the effects of magnetic order on the DOS and predicted photoelectron spectra, we compared the Fe(1) and O(1) partial densities for the superlattice structure (D_{3d}) and for O_h symmetry. For the $3d$ DOS [Fig. 2(b)] the position and magnitude of the main peaks is hardly changed. Less intense features, such as the shoulder at 1.5 eV and the 6.8-eV peak at the bottom of the ↑band, are unique to the D_{3d} cluster. For the O $2p$ DOS the dominant structures centered around 6.0 eV [Fig. 2(e)] are very similar. But within ± 3 eV of the Fermi energy, the $2p$ DOS of the D_{3d} cluster is very different from that with O_h symmetry. This is quite understand-

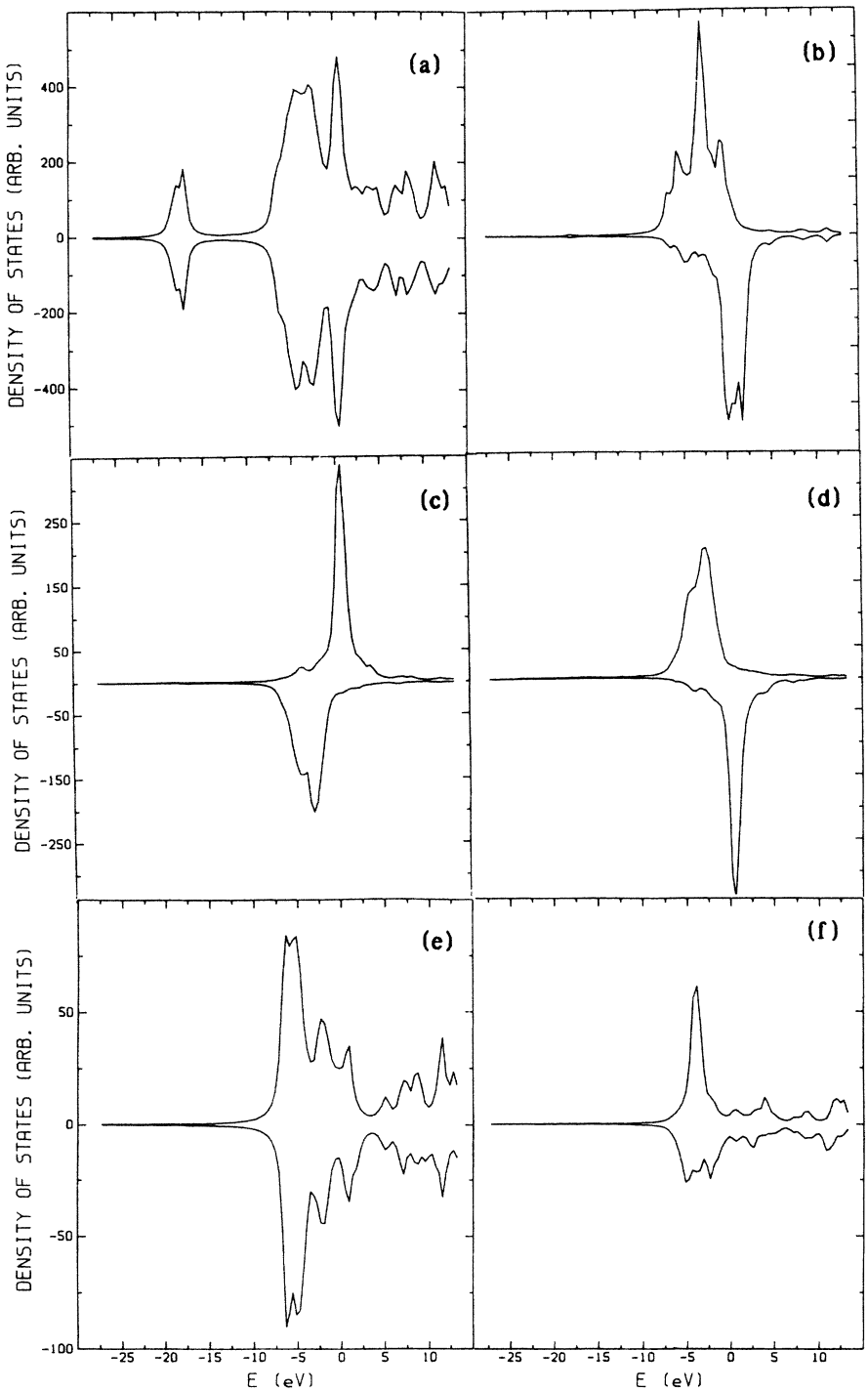

FIG. 2. Density of states (DOS) of the 27-atom cluster with D_{3d} symmetry. The zero of energy is E_F. The ↑-spin band is displayed above the abscissa, the ↓-spin is below it. (a) Total DOS, (b) $3d$ DOS of Fe(1↑) (the arrow here indicates the majority-spin direction), (c) $3d$ DOS of Fe(2↓), (d) $3d$ DOS of Fe(2↑), (e) $2p$ DOS of O(1), and (f) $2p$ DOS of O($2z$).

able, since in this region there is considerable spin-dependent mixing between O $2p$ and Fe $3d$ orbitals. In the AF D_{3d} case the ↑ and ↓ interactions are nearly in balance and a symmetrical DOS results. In the O_h case, there is necessarily a large spin imbalance leading to spurious peaks and ↑,↓ asymmetry in the O $2p$ distribution around E_F. Thus, if we are interested in properties which are strongly dependent on the detailed description of the electron orbitals within 3 eV of the Fermi energy, for example, the transport properties or semiconducting gap, for $T < T_N$, then the imposition of superlattice structure is essential. Of course, the necessity of using super-

lattices in band-theoretical calculations to even obtain a finite gap in magnetic insulators like MnO has been known for a long time.

2. *Effects of cation-interstitial defects*

Figure 3(a) gives the $3d$ DOS of Fe(1) in the T_d cluster with the first-shell oxygen atoms at 3.47 a.u. (unrelaxed position) from the interstitial iron atom. The DOS of (majority) spin ↓ has two well-defined peaks at 5.3 and 1.1 eV. As the first-shell oxygen-atom distance is increased to 4.16 a.u., the double peaks shifts to 5.0 and 2.9 eV, as shown in Fig. 3(b). This may represent an upper limit on the Fe—O bond relaxation, since the normal octahedral-coordination Fe—O bond length is 4.08 a.u. We can also see that the intensity of the peak at around 5.0 eV decreases, while the features become more sharp and atomiclike.

Figures 4(a) and 4(b) give the $2p$ DOS of O(1) placed at 3.47 and 4.16 a.u., respectively. Comparison of Fig. 2(e) with Fig. 4(b) shows that the dominant oxygen double peaks at 5.2 and 6.4 eV in octahedral coordination change to a single peak in 4:1 interstitial defect clusters. We can see that as the O(1)-Fe(1) distance increases, the $2p$ main-peak intensity increases, while the overall structure remains very similar. The oxygen DOS is thus not so sen-

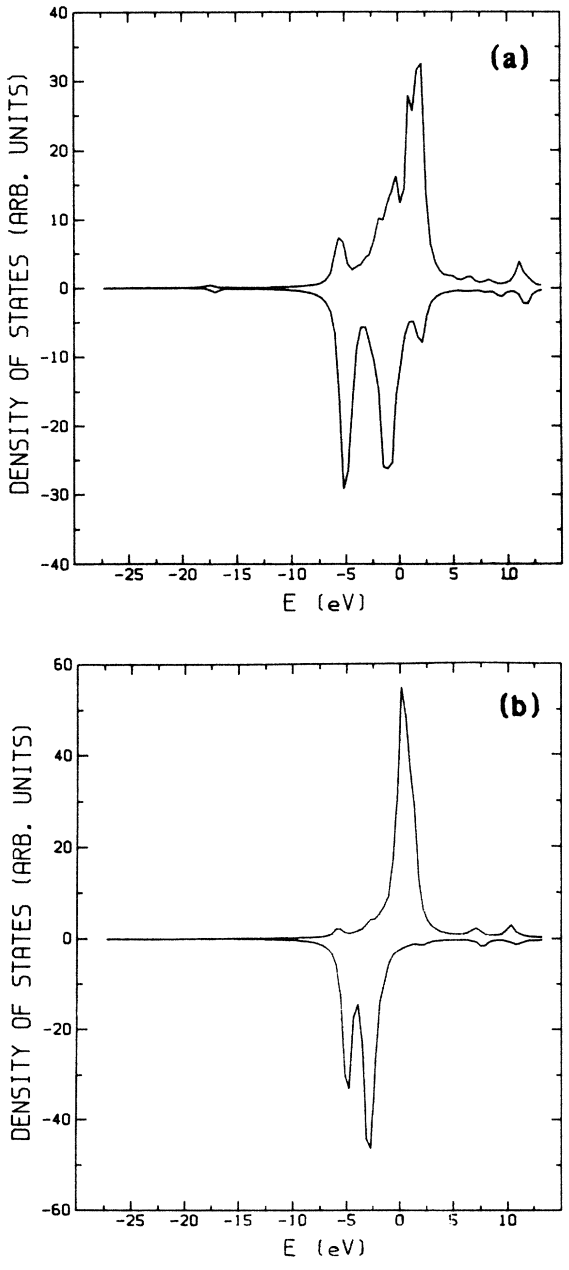

FIG. 3. $3d$ DOS of Fe(1↓) of the T_d interstitial cluster, for particular nearest- (R_1) and second-neighbor ($R_2=6.34$ a.u.) distances: (a) $R_1=3.47$ a.u. and (b) $R_1=4.16$ a.u.

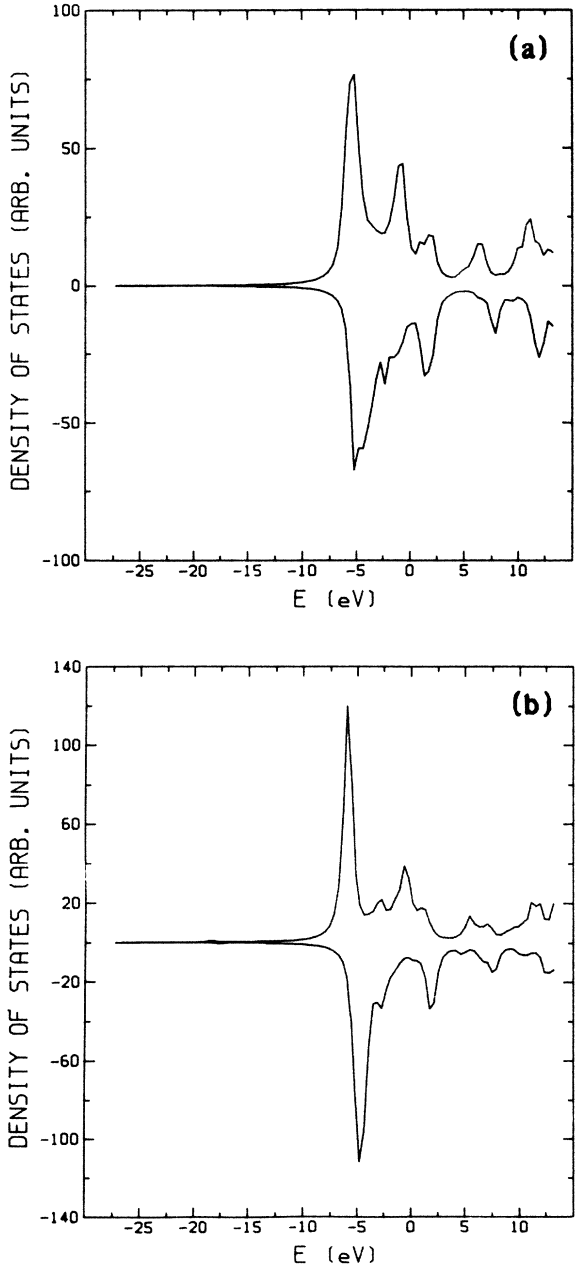

FIG. 4. $2p$ DOS of O(1) of the T_d cluster; distances as in Fig. 3. (a) $R_1=3.47$ a.u. and (b) $R_1=4.16$ a.u.

sitive to the immediate defect structure as the $3d$ DOS of the central Fe. In general, overlapping band features make it very difficult, if not impossible, to detect specific defect-related features in optical and photoelectron data.

C. XANES results

K-edge XANES of Fe contains considerable information about the local environment, which is not easily obtained by other approaches. For cluster models of muffin-tin–type potentials, shells of atoms can be deleted by substituting the corresponding atomic-sphere potentials by spheres of constant potential (i.e., V_{MT}). We can thus identify the effects of particular scattering events, within the first two shells of neighbors to the central-iron atom. The major parameters of our muffin-tin cluster potentials are listed in Table IV. Figures 5(a) and 5(b) show the effects of neighboring-atom shells and local symmetry on the XANES of central iron. We can see the following:

(a) The chemical environmental effects are clearly shown in the "single-Fe" XANES results. Since the central-iron-atom "ionicity," as defined by volume-integrated charge, changes from 1.15 in the O_h cluster to around 2.6 in the T_d cluster, charge transfer is a clear indication that the potential of the central site in the O_h cluster is more attractive than that of the T_d cluster. This is consistent with the Fe^{3+} valence state of the tetrahedral site in Fe_3O_4 and the mixed valence of the magnetite octahedral sites. One consequence is that the single-Fe XANES curve of iron in O_h symmetry shows a steeper shoulder than that of the T_d cluster.

(b) As the first-shell oxygen atoms are added, the XANES of Fe in both T_d and O_h clusters show a strong "shape resonance" at an energy around 20–35 eV above the muffin-tin zero. (Hereafter, we have set the zero at the muffin-tin constant V_{MT}.) Additionally, a strong preedge peak shows up in the T_d cluster and not in the O_h cluster. This point will be discussed later.

(c) As both the first-shell oxygen, O(1), and second-shell iron atoms, Fe(2), are included in the T_d cluster [the dashed-dotted line in Fig. 5(b)], we see that the second-neighbor iron has relatively weak effects on the XANES structure for $E > 15$ eV. However, there appear two preedge peaks. From further calculations (see below) we can see that the first preedge is associated with the $3d$ resonance of the neighboring iron atoms and the second preedge originates from central-iron $4p$-$3d$ mixing.

(d) As we add both the first- and second-shell oxygen atoms [the solid line in Fig. 5(b)], the second preedge persists, while the first preedge almost disappears. Also, the second-shell oxygen atoms dramatically modify the XANES of Fe in the T_d clusters for energy $E > 10$ eV.

(e) As we add both first-shell oxygen and second-shell Fe atoms to the O_h cluster [the solid line in Fig. 5(a)], the

TABLE IV. Muffin-tin potential parameters for cluster models employed in the K-edge iron XANES calculations. (OS denotes outer sphere.)

Cluster	FeO_6Fe_{12}	FeO_4O_{12} or FeO_4Fe_{12}
OS MT radius (a.u.)	8.02	8.74
Fe MT radius	2.25	2.10
O MT radius	2.25	2.10
V_{MT} (Ry) (spin up)	−1.00	−0.75
(spin down)	−0.99	−0.74
OS L_{max}	15	12
Fe(1) L_{max}	5	5
O(1) L_{max}	2	3
Fe(2) or O(2) L_{max}	3	2

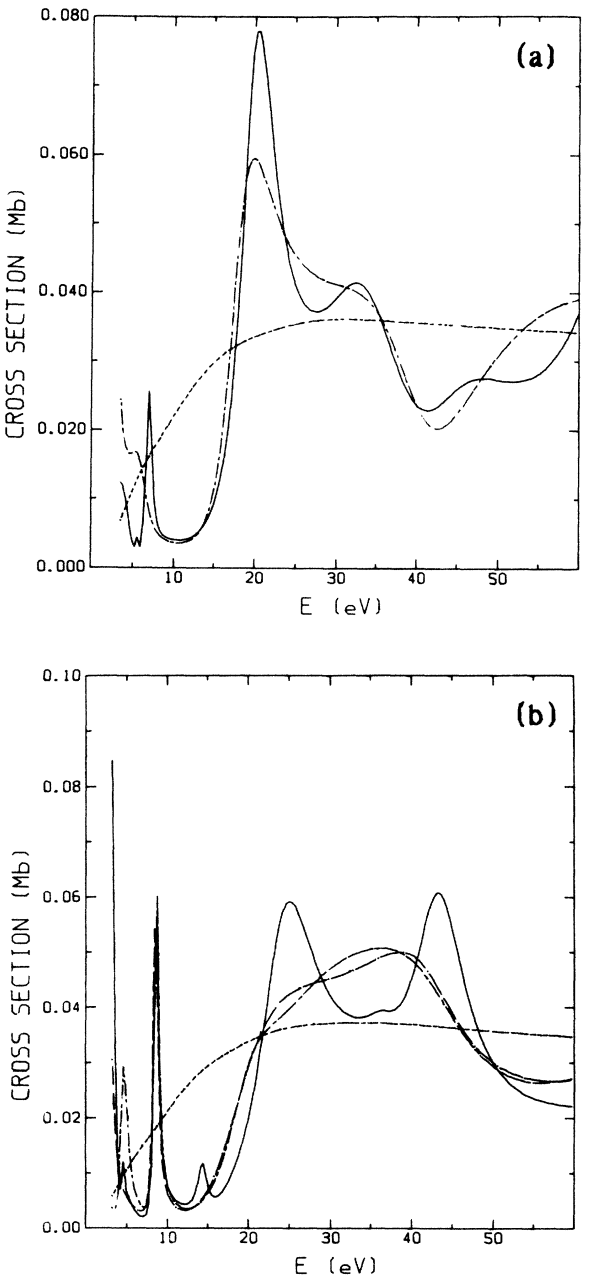

FIG. 5. Effects of the first few nearest-neighbor atom shells and local symmetry on the XANES of Fe. (a) O_h clusters: isolated Fe (dotted line), FeO_6 (dashed-dotted line), and FeO_6Fe_{12} (solid line). (b) T_d clusters, with $R_1 = 3.82$ a.u., $R_2 = 6.64$ a.u.: isolated Fe (dotted line), FeO_4 (dashed line), FeO_4Fe_{12} (dashed-dotted line), and FeO_4O_{12} (solid line).

overall XANES develops more detailed structure; also a preedge peak appears. Since the potential of the O_h cluster has inversion symmetry with respect to the central-iron atom, it is impossible to have any preedge peak associated with the $4p$-$3d$ mixing of the central iron. Thus the preedge seen in Fig. 5(a) can only be related to the $3d$ resonance of the neighboring iron, Fe(2).

We observe that the neighboring iron atoms, either in T_d or O_h clusters, do not affect the central-atom K-edge XANES as much as the neighboring oxygen atoms. We can see that at near-edge energies the low-Z neighboring ion has much stronger scattering effects on the photoelectron than high-Z atoms.[24] This may be one of the major reasons that single-scattering extended x-ray-absorption fine-structure (EXAFS) calculations can reproduce the accurate band-structure-calculated XANES of Cu from 200 eV down to the edge,[25] while the single-scattering approximation failed for NiO.[26] The strong-scattering neighboring oxygen atoms in NiO make the multiple-scattering effects non-negligible near the threshold. Recent work of Rehr *et al.*[27] supports this argument.

Figure 6 shows evidence of iron p-d mixing in the T_d cluster $FeX_4O_4O_{12}$, with $R_1=3.47$ a.u. and $R_2=6.34$ a.u. The preedge peak around 9 eV disappears as we exclude the $l=2$ partial-wave final-state contribution in the XANES calculations. There are additional peaks at around 4.5 eV, but since the Fermi energy for the T_d cluster is around 7 eV, these bound-bound transitions are forbidden by the Pauli exclusion principle.

Figures 7(a) and 7(b) show the spin dependence of Fe XANES. The spin distribution is mainly localized on the Fe $3d$ electron, while s and p states are primarily involved in the x-ray absorption. The d-p mixing only exists for metal sites without inversion symmetry, i.e., in T_d but not the O_h clusters; thus, the stronger spin dependence of $\sigma(\omega)$ appears in the T_d case. The occurrence of $\uparrow,\downarrow$ preedge peaks at *different* energies in the O_h cluster is an artifact of the imposed symmetry. The $\sim$3-eV $\downarrow$ splitting seen in T_d symmetry is due to sharp ligand-field features in the DOS (see Fig. 3).

Figure 8 shows the effects of bond-length changes on the Fe XANES. Here we can see that, as the first-shell oxygen distance increases, the intensity of the preedge peak at $10<E<15$ eV increases, while the Fe p-d peak around 9 eV changes very little. For $E>20$ eV the peak

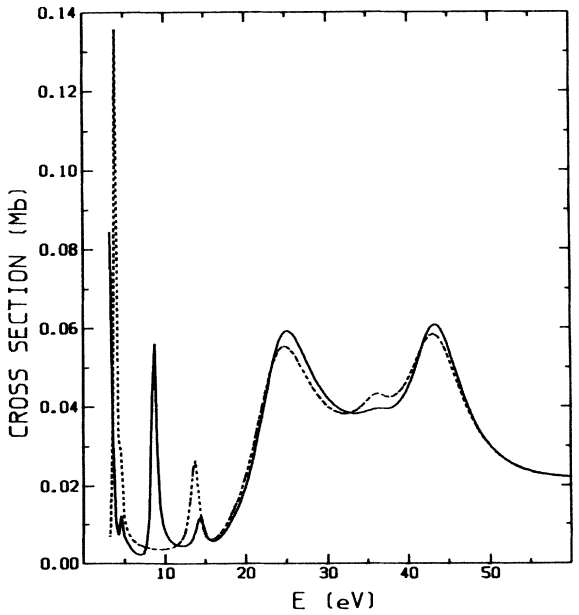

FIG. 6. Evidence for Fe p-d mixing in the T_d cluster $FeX_4O_4O_{12}$, where the solid line denotes the full cross section and the dotted line gives the cross section with the Fe $l=2$ partial wave omitted from the final-state expansion.

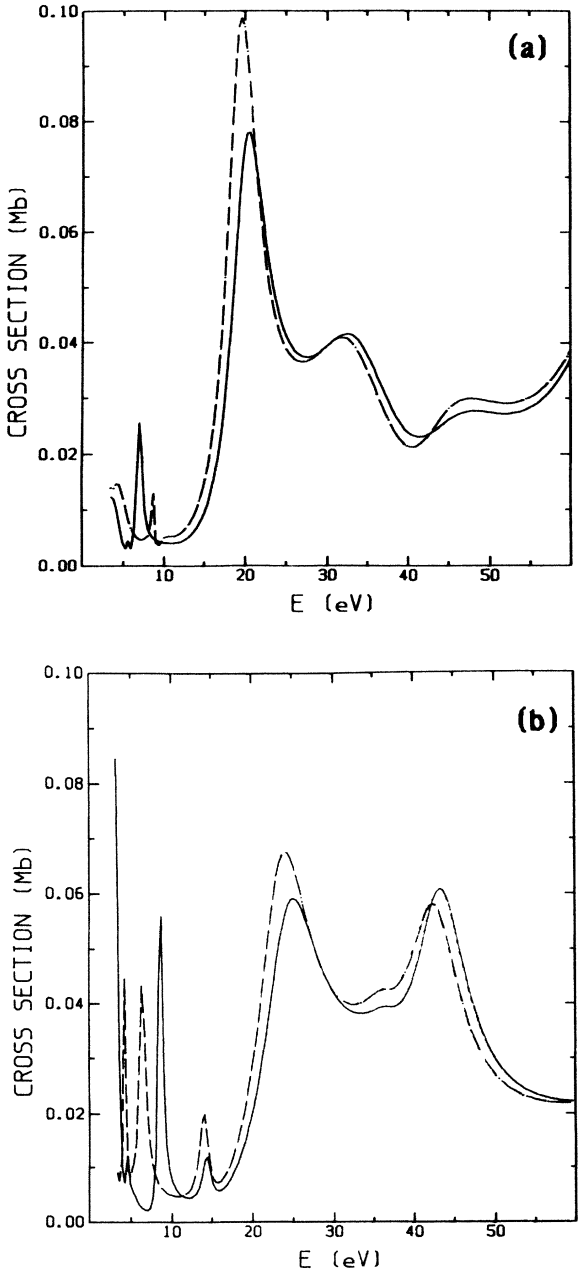

FIG. 7. Spin dependence of iron K-edge XANES [solid (dashed) lines indicate spin up (down)], (a) FeO_6Fe_{12} (O_h) and (b) $FeX_4O_4O_{12}$ (T_d).

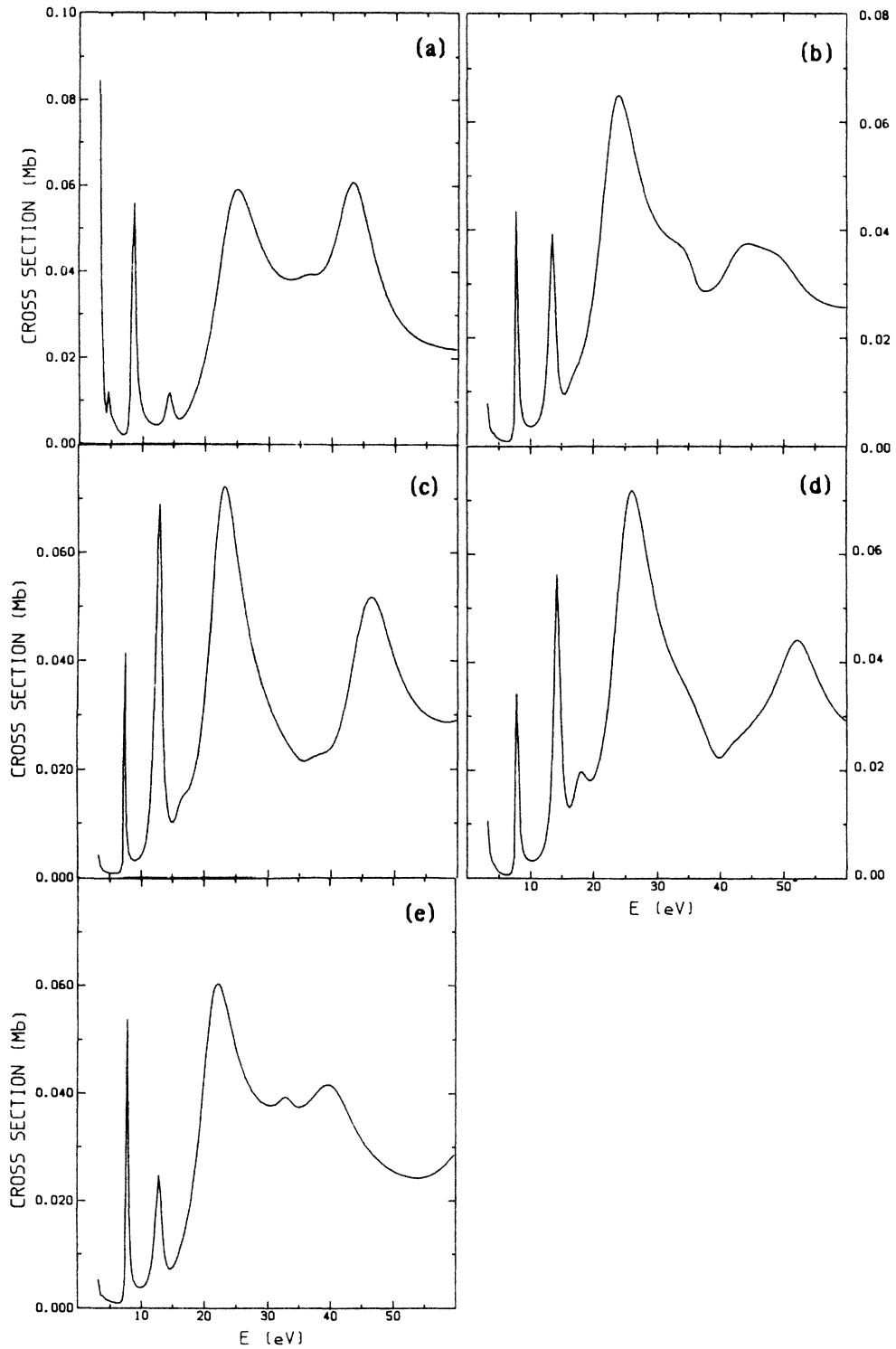

FIG. 8. Effects of first- and second-neighbor bond lengths on K-edge XANES in $FeX_4O_4O_{12}$ (T_d symmetry): $R_2=6.34$ a.u. and (a) $R_1=3.47$, (b) 3.82, and (c) 4.16 a.u.; $R_1=3.82$ a.u. and (d) $R_2=6.05$, (b) 6.34, and (e) 6.64 a.u.

positions vary roughly inversely with the second-shell oxygen distances. However, multiple-scattering effects involve the nearest-neighbor oxygen as well.

In order to estimate the observable effects of the 4:1 defect cluster in wustite, we superimpose the "perfect-crystal" K-edge and the T_d results in Fig. 9. We see that both sites have a sharp preedge peak as discussed above; however, the second peak of the defect cluster at around 15 eV probably would show up as a shoulder on the low-energy side of the main peak. In addition, the main peak of the defect cluster, as compared to the mean peak of the perfect crystal, shifts to higher energy (in this case, by 4.7

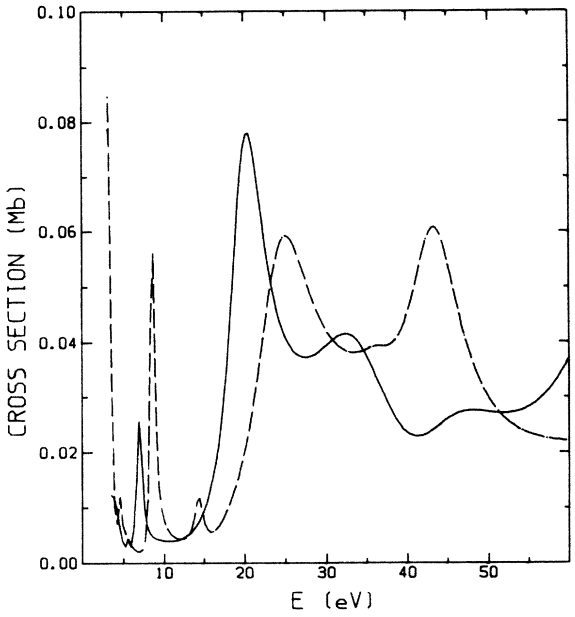

FIG. 9. K-edge XANES of iron in wustite. Solid line, normal octahedral site; dashed line, tetrahedral metal interstitial site, $R_1 = 3.47$ (a.u.), $R_2 = 6.34$ a.u.

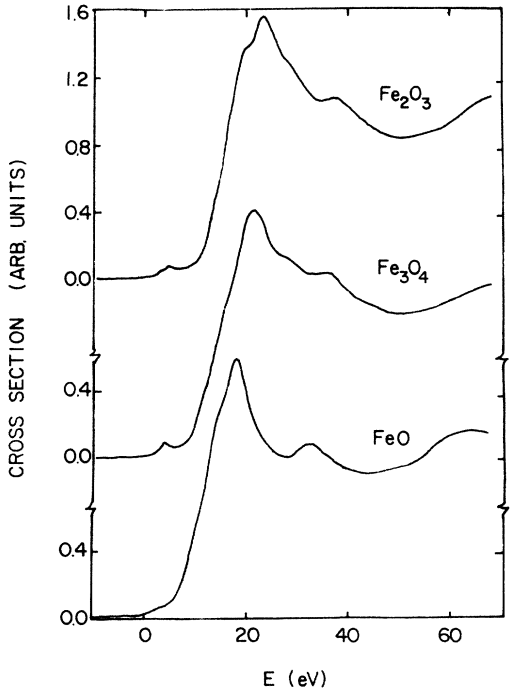

FIG. 10. Experimental results of K-edge XANES of iron in FeO, Fe_3O_4, and Fe_2O_3 (Refs. 6 and 20).

eV). About half of the shift can be accounted for by difference in bond lengths. This will result in broadening the main peak on the high-energy side, with a possible visible shoulder.

Figure 10 shows the experimental results of Bunker[6,20] for K-edge XANES of iron in FeO, Fe_3O_4, and Fe_2O_3. Obviously, we can see that in the iron oxide compounds with larger [O]/[Fe] ratio, the main peak broadens and shifts to higher energy; also, it shows more clear shoulder structure at the low-energy side of the main peak. Although the crystal structure of Fe_3O_4 and Fe_2O_3 does not really model the defect lattice $Fe_{1-x}O$, the connection between the tetrahedral site in magnetite and the 4:1 defect is rather close.

IV. CONCLUSIONS

From DVM calculations, we found that as the wustite cluster symmetry changes from O_h (ideal structure) to T_d (4:1 defect), the central-iron volume charge increases by $1.4e$, while the net spin increases by 0.7. This is consistent with many previous suggestions that high-spin ferric ions preferentially occupy the interstitial T_d sites.

The importance of imposing superlattice structure has been studied in terms of charge distribution, magnetization, and DOS. We conclude that the superlattice is essential for an accurate determination of Fe $3d$ or O $2p$ spin distributions, and detailed peak structure of the DOS within 3 eV of the Fermi energy, while most other features are stable. The calculated magnetic moments are significantly smaller than previous estimates used in fitting neutron data, due to covalent bonding with oxygen ligands. Since the cluster values of $(3.2-3.8)\mu_B$ are probably an *overestimate,* it would be worthwhile to reconsider hypotheses about local defect-cluster magnetization which were invoked to fit experiment.

In a perfect crystalline cluster, the $3d$ DOS of iron has four peaks and the O $2p$ DOS has double peaks at around 6 eV from the Fermi energy, in reasonable agreement with x-ray-photoemission-spectroscopy (XPS) data. In 4:1 interstitial defect clusters, the majority-spin DOS of Fe $3d$ exhibits ligand-field-split double peaks, with an energy difference of 2—4 eV, depending on the Fe-O distance.

As for the K-edge XANES of iron, we found the following:

For the octahedral environment, the overall cross-section shape is determined by the first-shell oxygen atoms, due to "shape-resonance" or "molecular-cage effects." Neighboring iron atoms have relatively weak scattering effects for photoelectrons with energy larger than 15 eV. A preedge structure is interpreted as originating from the coupling of the $4p$ partial wave of the central Fe with the $3d$ resonance of the neighboring iron atoms, not from symmetry-forbidden $4p$-$3d$ mixing. The cross section has a very weak spin dependence.

For the interstitial 4:1 defect clusters, the main peak shifts 3.3—8.4 eV to higher energy, as compared with the main-peak position in the O_h cluster, depending on the local oxygen bond-length relaxations. The lack of inversion symmetry allows central-iron $4p$-$3d$ mixing, leading to a preedge peak, in addition to the peak originating from the neighboring iron $3d$ resonance. The intensity of this peak is inversely related to the strength of the Fe—O bonding interaction. The structures above the main peak ($E > 15$

eV) are rather sensitive to the location of the second-shell oxygen atoms. The preedge peak locations and intensities are determined by the first-shell oxygen Fe-O distance. We suggest that the shoulder on the low-energy side of the main K-edge peak of the 4:1 defect is associated with multiple scattering between the first- and second-shell oxygen atoms.

From both experimental and theoretical studies, it is clear that for transition-metal oxides the preedge region of XANES is sensitive to both charge transfer and local symmetry. The dominant structures above the main peak are sensitive mainly to the Fe—O(1) and Fe—O(2) bond lengths. Our theoretical results not only show explicitly the iron $4p$-$3d$ mixing in T_d clusters, but we also can qualitatively explain the shifting of the location of the main peak as well as the appearance of shoulders observed in the K-edge XANES of iron in oxygen-rich iron oxide compounds. We suggest that XANES measurements on $Fe_{1-x}O$ with different (known) defect concentrations could be useful to determine the local-defect bond distances.

ACKNOWLEDGMENTS

We thank Grant Bunker for allowing us access to his unpublished XANES results for FeO, Fe_2O_3, and Fe_3O_4. We also thank F. W. Kutzler, M. R. Press, J. B. Cohen, and T. O. Mason for many helpful discussions. This work was supported by the U.S. Department of Energy under Grant No. DE-FG02-84ER45097.

[1]M. Hayakawa, J. B. Cohen, and T. B. Reed, J. Am. Ceram. Soc. **55**, 160 (1972).

[2]F. Keffer, *Handbuch der Physik,* edited by H. P. J. Wijn (Springer, New York, 1966), Vol. 18, Pt. 2.

[3]H.-C. Chen, E. Garstein, and T. O. Mason, J. Phys. Chem. Solids **43**, 991 (1982).

[4]F. B. Koch and J. B. Cohen, Acta Crystallogr. Sect. B **25**, 275 (1969); E. Gartstein and T. O. Mason, J. Am. Ceram. Soc. **65**, C24 (1982).

[5]F. W. Kutzler, D. E. Ellis, T. I. Morrison, G. K. Shenoy, P. J. Viccaro, P. A. Montano, E. H. Appelman, L. Stein, M. J. Pellin, and D. M. Gruen, Solid State Commun. **46**, 803 (1983); F. W. Kutzler and D. E. Ellis, Phys. Rev. B **29**, 6890 (1984).

[6]L. A. Grunes, Phys. Rev. B **27**, 2111 (1983); G. G. Bunker, Ph.D. thesis, University of Washington, Seattle, 1983 (unpublished).

[7]N. N. Greenwood and A. T. Howe, J. Chem. Soc. (Dalton Trans.) **1**, 110 (1972); **1**, 116 (1972); **1**, 122 (1972), and references therein.

[8]S.-H. Chou, F. W. Kutzler, D. E. Ellis, G. K. Shenoy, T. I. Morrison, and P. A. Montano, Phys. Rev. B **31**, 1069 (1985).

[9]E. J. Baerends, D. E. Ellis, and P. Ros, Chem. Phys. **2**, 41 (1973).

[10]A. Rosén, D. E. Ellis, H. Adachi, and F. W. Averill, J. Chem. Phys. **65**, 3629 (1976); D. E. Ellis and G. S. Painter, Phys. Rev. B **2**, 2887 (1970).

[11]D. E. Ellis, G. A. Benesh, and E. Byrom, J. Appl. Phys. **49**, 1543 (1978); Phys. Rev. B **20**, 1198 (1979), V. A. Gubanov, A. L. Ivanovsky, G. P. Shveikin, and D. E. Ellis, J. Phys. Chem. Solids **45**, 719 (1984).

[12]P. D. Battle and A. K. Cheetham, J. Phys. C **12**, 337 (1979), and references therein.

[13]I. Balberg and H. L. Pinch, J. Magn. Magn. Mater. **7**, 12 (1978); D. Adler and B. H. Auker, J. Solid State Chem. **12**, 355 (1975).

[14]R. S. Mulliken, J. Chem. Phys. **23**, 1833 (1955); **23**, 1841 (1955).

[15]J. L. Dehmer, J. Chem. Phys. **56**, 4496 (1972); D. Dill and J. L. Dehmer, *ibid.* **61**, 692 (1974); J. L. Dehmer and D. Dill, *ibid.* **65**, 5327 (1976).

[16]C. R. Natoli, F. W. Kutzler, D. K. Misemer, and S. Donaich, Phys. Rev. A **22**, 1104 (1980).

[17]F. W. Kutzler, C. R. Natoli, D. K. Misemer, S. Doniach, and K. O. Hodgson, J. Chem. Phys. **73**, 3274 (1980).

[18]F. W. Lytle, D. E. Sayers, and E. A. Stern, Phys. Rev. B **11**, 4825, 4836 (1975).

[19]V. O. Kostroun, M. H. Chen, and B. Crasemann, Phys. Rev. A **3**, 533 (1971).

[20]G. C. Bunker (private communication).

[21]D. E. Eastman and J. L. Freeouf, Phys. Rev. Lett. **34**, 395 (1975).

[22]S. F. Alvarado, M. Erbudak, and P. Munz, Phys. Rev. B **14**, 2740 (1976).

[23]G. Grenet, Y. Jugnet, T. M. Duc, and M. Kibler, J. Chem. Phys. **72**, 218 (1980); **74**, 2163 (1981).

[24]B. K. Teo and P. A. Lee, J. Am. Chem. Soc. **101**, 2815 (1979).

[25]J. E. Muller and W. L. Schaich, Phys. Rev. B **27**, 6489 (1983).

[26]D. Norman, J. Stohr, R. Jaeger, P. J. Durham, and J. B. Pendry, Phys. Rev. Lett. **51**, 2052 (1983).

[27]J. J. Rehr and R. C. Albers (unpublished).